Investigating Grease Behaviour in Tilted Double-Row Tapered Roller Bearing Installed in Wind Turbine by Developing a Full Scale Multi-Phase CFD Model

Muhammad Ishaq Khan, Lorenzo Maccioni, and Franco Concli

Faculty of Engineering, Free University of Bozen-Bolzano, 39100 Bolzano, Italy.

Correspondence: Lorenzo Maccioni (lorenzo.maccioni@unibz.it)

Abstract. Lubrication plays critical role in effective performance of Tapered Roller Bearings (TRBs) used as main-bearing in wind turbines. Several experimental and CFD-based studies have investigated lubrication behaviour in single-row TRBs. However, grease-lubricated double-row TRBs have not yet been studied extensively, particularly in large size bearings. There-fore, this paper aims to investigate in detail the grease behaviour in a tilted double-row TRB installed in direct-drive wind turbine by developing a novel, full scale, multiphase CFD model. This model was implemented in open-source environment OpenFOAM®, using a transient, incompressible solver. The grease was modeled as a non-Newtonian fluid using the Herschel-Bulkley formulation, with its rheological parameters determined by performing a best-fit analysis on experimentally obtained data. The simulated operating conditions included three grease filling ratios—45 %, 35 %, and 21 % of total volume of bearing lubricating chamber—at rated rotational speed i.e. 17.5 rpm with a bearing tilt of 5° towards the Main-Frame Side (MFS) w.r.t the vertical axis. The results highlight the grease flow characteristics including grease distribution, fluxes, and pressure fields within the bearing after one complete rotation of cage at the stated operating conditions. They emphasize that the lubricant behavior inside the bearing is strongly affected by the combined influence of bearing tilt and gravitational forces.

1 Introduction

The generation of electricity from conventional energy sources, such as fossil fuels, has significantly contributed to the rise in global temperatures, resulting in global warming and increasingly severe environmental conditions (Ren et al., 2024). Accord-ing to UN Climate Change 2022 Report, Earth has witnessed the highest levels of green house gases (GHG) emissions over the past decade (Intergovernmental Panel on Climate Change, 2022). Consequently, the transition to renewable energy sources is imperative to ensure the sustainable development of the planet. Among various renewable energy sources, wind energy has emerged as one of the most penetrated and abundant sources of clean energy (Kaymaz et al., 2021). Therefore, the efficient and reliable operation of wind turbine is critical for ensuring the sustainability of renewable energy systems (Torwey and Mendelin, 2025).

Bearings are essential machine elements that play significant role in enabling efficient rotation in any mechanical system. They can carry radial and axial loads during operation (Hong and Tong, 2016). Tapered Roller Bearing (TRB) is one of the

most widely used types of bearings in wind turbines, automotive transmissions, and heavy machineries, due to its ability to
25 support combined radial and axial loads (Tong and Hong, 2014). In particular, double-row Tapered Roller Bearing (TRB) is
used to carry higher radial and axial loads as compared to single-row TRB. It supports loads in multiple directions (Bercea
et al., 2003). Wind turbines are subjected to substantial loads due to their large and tall structures, as well as the variability in
wind speed. Therefore, double-row TRB are most commonly used as main bearing in wind turbines to support these high loads
and provide better mechanical integrity.

30   Effective lubrication is one of the key factors in maximizing the service life of bearing and ultimately any mechanical
system (Khonsari and Booser, 2017). Lubricant distribution inside bearing makes it possible to minimize heat generation and
also rapidly dissipates the heat generated (Mang and Dresel, 2007). Thus, keeping the bearing temperature in operating range
reducing the losses due to friction known as load dependent power losses (P_{LB_P}). However, lubrication also contributes to the
power losses that are due to viscous (drag) and inertial (churning) effects during its interaction with rolling elements (Niemann
35 and Winter, 2002). These losses are called load independent power losses (P_{LB_o}).

      Eco-friendly and sustainable developments aim to develop efficient systems (Zhang, 2013). The advancement in computer
technology paved the way to achieve the stated objective. Computational Fluid Dynamics (CFD) is one of the tools to study
and optimize the lubrication behaviour and its key aspects inside bearing (Versteeg, 2007). Several CFD studies have been
performed focusing lubrication in bearings from the last decade (Maccioni and Concli, 2020). CFD tool was used to estimate
40 drag coefficient of roller in cylindrical rolling bearing exploring single phase model by Marchesse et al. (2019), and Gao et al.
(2022b). A multiphase solver was used to simulate single sector of oil-lubricated cylindrical roller bearing for estimation of
(P_{LB_o}) by Concli et al. (2020) and Feldermann et al. (2017). Deng et al. (2022) combined CFD and non-linear dynamic models
to analyze the oil-air flow and temperature in ball bearings. Chen et al. (2023) performed CFD simulation of single sector to
study oil-air flows in ball bearings. Raju et al. (2013) simulated two different oil inlet positions in needle roller bearing to give
45 optimum position for oil inlet. Multiphase simulation was performed by Crouchez-Pillot and Morvan (2014) capturing the
behaviour of two immiscible fluids i.e., oil and air inside bearing. They used Volume of Fluid (VoF) model for their study. This
model was used Hu et al. (2014) and developed transient model to simulate oil-gas phases in angular contact ball bearing. Gas
flows in roller bearing were simulated under varying speed and cage structure by Sun et al. (2014).

      Several CFD studies have been applied to TRBs. Liebrecht et al. (2015, 2017) performed study to find the influence of
50 oil quantity on total friction in TRB with vertical axis of rotation. Gonda et al. (2018, 2019) studied TRB having horizontal
axis of rotation to calculate resistant torque under varying speed, oil levels, and temperature. Oil flows in 32312-A TRB were
simulated by Maccioni et al. (2022b) studying the aeration impact on oil behaviour inside bearing. A numerical model was
validated against experimental study by Maccioni et al. (2022a). P_{LB_o} were investigated by Maccioni et al. (2023b) in TRB
by numerical and experimental study. Few studies have also been reported applying CFD to double-row TRBs. Li et al. (2022)
55 studied double-row TRB during loss of lubrication process via CFD. Zhu et al. (2022) the effect of different rib structure on
oil fluxes by using CFD tool.

      Experimental studies have been conducted to study lubrication phenomenon in rolling bearings. Wu et al. (2016) performed
experimental study for predicting oil flow behaviour and thermal characteristics in jet lubricated ball bearings employing high

speed imaging technique. Wen and Oshima (2014) and Santhosh et al. (2017) used transparent surfaces and macroscopically observed the affect of cage designs on oil splashing behaviour and patterns in ball bearings. Russell et al. (2021) developed a novel test rig to study the frictional characteristics for different cage designs in deep grove ball bearings. Aamer et al. (2022) extended the work of Russell et al. (2021) by modifying the test rig for optical visualization and also performed CFD analysis for predicting oil distribution.

Experimental investigations have also been carried out on TRBs. Electrical Impedence Spectroscopy (EIS) technique was used to estimate lubricant film thickness (Manjunath et al., 2024). Maccioni et al. (2022a) developed a test rig to analyze the lubricant behaviour in TRB using Particle Image Velocimetry (PIV) technique. In this study, it was found that bubble formation in oil increases with the rotational speed of bearing. In another study, Maccioni et al. (2023a) , employing PIV method captured velocity fields in different regions in fully flooded oil lubricated TRB. Hoeprich (2005) studied grease behaviour in TRB experimentally. Gao et al. (2022a) experimentally studied the thermal characteristics of railway double-row TRB by varying the rotational speed. It was shown that the difference in temperature narrows down between inner and outer rings with the increase in rotational speed.

Based on the study performed by Ishaq Khan et al. (2025) , it is witnessed that most experimental and numerical studies have been limited to oil-lubricated single-row TRB. Furthermore, the TRBs that were studied had an Outside Diameter (OD) less than 300 mm. No comprehensive study has been reported for grease-lubricated double-row TRB at such a large scale. It is also worth mentioning that the simulation models developed in the above studies employed a symmetry-based approach—simulating only a single sector and extrapolating the results to represent the entire bearing—except for the work by Concli et al. (2020). However, the use of symmetry is not always valid. In the present study, the double-row tapered roller bearing (TRB), installed in a wind turbine with a bore diameter of 1780 mm, is tilted by $5°$ towards the Main-Frame Side (MFS) w.r.t the vertical axis. As a result, each sector of the bearing experiences different loading and lubrication conditions. To reliably capture the underlying physics, it is essential to investigate the behavior of the grease-lubricated double-row TRB in detail under varying operating conditions.

In the light of this, the objectives of this paper are:

1. To develop a novel, full scale, multiphase, 3-D CFD model in OpenFOAM® environment for tilted double-row TRB.

2. To investigate the behaviour of grease inside bearing under varying operating conditions.

2 CFD Model Development

2.1 Geometry of Double-Row TRB

The development of CFD model for 41513219[1] double-row TRB started from the detailed study of its geometry. The main components of the bearing are rollers, cage, seal, inner raceway, and outer raceway. The 3-D CAD model of the bearing is shown in the Fig. 1a and the main components are highlighted in the section view of the bearing as shown in Fig. 1b. Each row

---

[1]This number represents the bearing reference code.

90 consists of 65 identical sectors making total of 130 similar sectors. The roller was scale down by a factor of 0.98 with respect to its center of gravity to create clearance between roller and raceways. The key geometric specifications of the bearing are listed in Table 1.
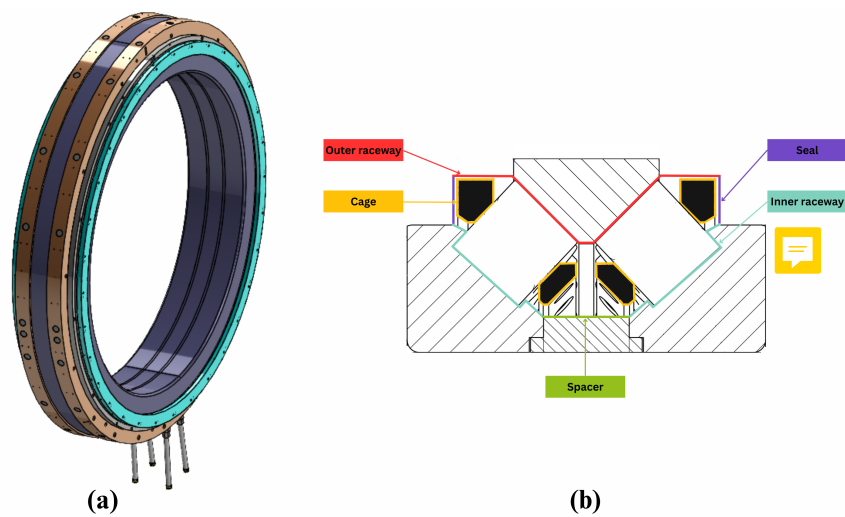
Figure 1. 41513219 double-row TRB **(a)** 3-D CAD model **(b)** Section view

Table 1. Key parameters of the bearing

Parameter	Value
Type	Double-Row TRB
Outer Diameter	1780 mm
Bore Diameter	1370 mm
Pitch Diameter	1566 mm
Width (total)	276 mm
Mean Diameter of Roller	68 mm
Number of Rollers (total)	130

2.2 Meshing of Double-Row TRB

2.2.1 Meshing of Half Sector

95 The bearing exhibits geometric symmetry and a periodic structure, which greatly facilitate the meshing process for the entire model. A systematic approach to initiate the meshing process was to first generate the mesh for a fraction of the entire domain—specifically, half of a single representative sector. The mesh of the entire bearing was then generated by systemati-

cally rotating the half-sector mesh around the bearing axis. This method simplifies the meshing process by making use of the bearing's repeating pattern, which not only reduces complexity in the initial setup but also makes the overall workflow more manageable.

The half sector was divided into 7 partitions at the lateral side, while the front side was segmented into 23 parts with specific pattern as shown in Fig. 2. This pattern was consistently applied across all 7 lateral partitions of the half sector. It enabled the creation of high-quality structured mesh exploiting the blockMesh utility in OpenFOAM®. Hexahedral blocks were created to ensure maximum numerical accuracy, with each block consist of 8 vertices and its width spanning between adjacent partitions. There were total of 123 blocks created in this half sector.
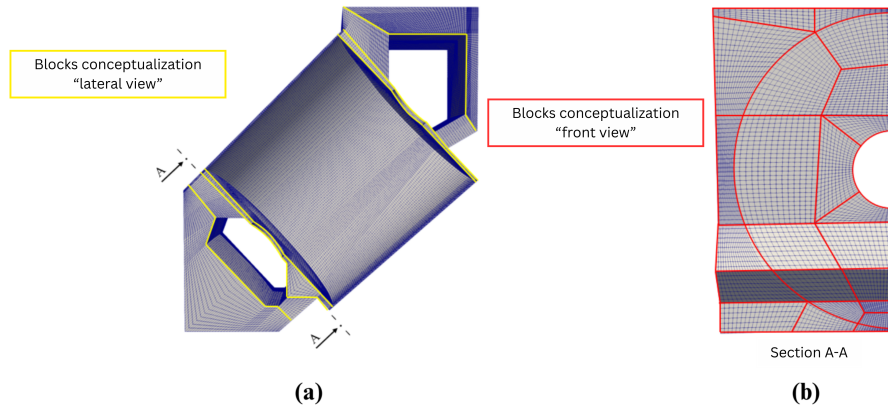
Figure 2. Mesh of the half sector **(a)** Lateral view **(b)** Front view

2.2.2 Meshing of Full Bearing

The creation of mesh for the entire bearing presented a significant challenge. The symmetry and periodic nature of the bearing were utilized to generate the mesh for the entire model. The previously created half-sector mesh served as the reference, which was systematically rotated through $360°$ around the bearing axis (x-axis) to construct the complete bearing mesh. The rotation was performed in the y–z plane using a standard rotation matrix as shown in Eq. 1.

$$\mathbf{R}_x = \begin{bmatrix} 1 & 0 & 0 \\ 0 & \cos\alpha & -\sin\alpha \\ 0 & \sin\alpha & \cos\alpha \end{bmatrix} \tag{1}$$

In this context, α represents the rotation applied to each vertex of the half-sector mesh. Since each bearing row consists of 65 identical sectors, the angular width of each sector is:

$$\alpha = \frac{360°}{65} = 5.53°$$ (2)

115 Each vertex is represented by a 3-D coordinate vector as:

$$\mathbf{v} = \begin{bmatrix} x \\ y \\ z \end{bmatrix}$$ (3)

A MATLAB® script was developed to implement this logic, which parametrically generated the vertices, blocks, arcs, and patches for the entire bearing. The script first created the second half of the initial sector by mirroring the z-coordinates of the original vertices with respect to the x–y plane, while keeping the x and y coordinates unchanged. This resulted in two adjacent

120 half-sectors forming one complete sector within the same row, symmetrically reflected across the x–y plane.

To complete a full 360° rotation and generate the mesh for the entire bearing, the coordinates of each vertex of this sector were rotated by $5.53°$ in successive steps around the bearing axis in the y–z plane. For the second sector, the vertex coordinates from the first sector were rotated by $5.53°$. For the third sector, the output coordinates from the second sector were again rotated by the same angle, and so on. This recursive approach ensured that each sector was generated based on the immediately

125 preceding one, simulating a cumulative rotation through the full circular geometry. However, certain vertices lying along the boundaries between adjacent sectors were common across sectors due to their symmetry. To preserve mesh continuity and avoid duplicate nodes at shared locations, the script reused these boundary vertices from the previous sector instead of creating new ones. This transformation was implemented via matrix-vector multiplication, as shown below:

$$\mathbf{v}_j^{(k)} = \begin{cases} \mathbf{v}_j^{(k-1)}, & \text{if } \mathbf{v}_j^{(k)} \text{ is a shared vertex from sector } k-1 \\ \mathbf{R}_x(\alpha) \cdot \mathbf{v}_j^{(k-1)}, & \text{otherwise} \end{cases}$$ (4)

130 Each transformation was executed in the script using a nested `for loop`, which iterated over all sectors, thereby constructing the complete mesh for 65 sectors within a single bearing row.

The bearing consists of two rows that are mirror images of each other. The symmetry were used to create the second row. To use mirror utility, `stl.` files were created in order to keep the patches for the second row as well. The first row was then mirrored through symmetry. This automated and parametric approach enabled the generation of a high-resolution, structured

135 hexahedral mesh for the full double-row tapered roller bearing geometry. The total cell count reached approximately 12.5 million. The grid for the full geometry is demonstrated in Figs. 3 and 4.

2.2.3 Patches of the Modelled Bearing

The division of mesh into different regions can be done by defining patches. Patch is the combination of boundary faces that defines a specific region inside computational domain. Different Boundary Conditions (BCs) are then applied to these patches
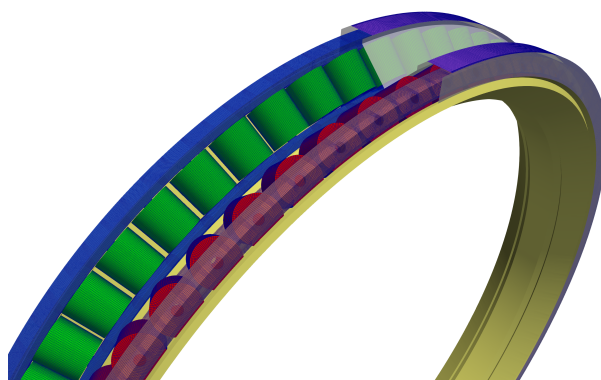
Figure 3. Grid visualization of patches Rollers, and Cages
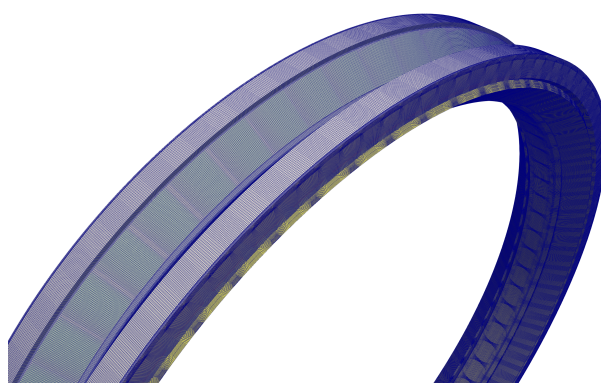
Figure 4. Grid visualization of patches InnerRing, InletOutlet, and OuterRing

140 according to the physical conditions. In this study, the entire mesh of double-row TRB was divided into several patches as shown in Fig. 5.

Each roller in left and right was defined as separate patch. The red color shows the rollers in left row while the green color shows the rollers in right row. Right and left cages are shown in blue and brown colors respectively. 'InletOutlet' patch in purple, 'InnerRing' in yellow, while 'OuterRing' is shown in transparent. Three additional patches—namely, AMI, PRES-

145 SURE, and WALLS—were defined to ensure appropriate pressure boundary conditions within fluid domain. These patches were superimposed on the outer surface of the 'InletOutlet' patch using mergeMeshes utility in OpenFOAM®.

2.2.4 Key Parameters of Mesh Quality

The mesh created for the full bearing was further check for its quality. The utility named checkMesh in OpenFOAM® used for this purpose. The key parameters of mesh quality are listed in Table 2. Aspect ratio of the mesh is the ratio of longest side of

150 the cell to the shortest side of the cell. For this mesh, max aspect ratio of 13.968 was acceptable. Skewness of the cell is the
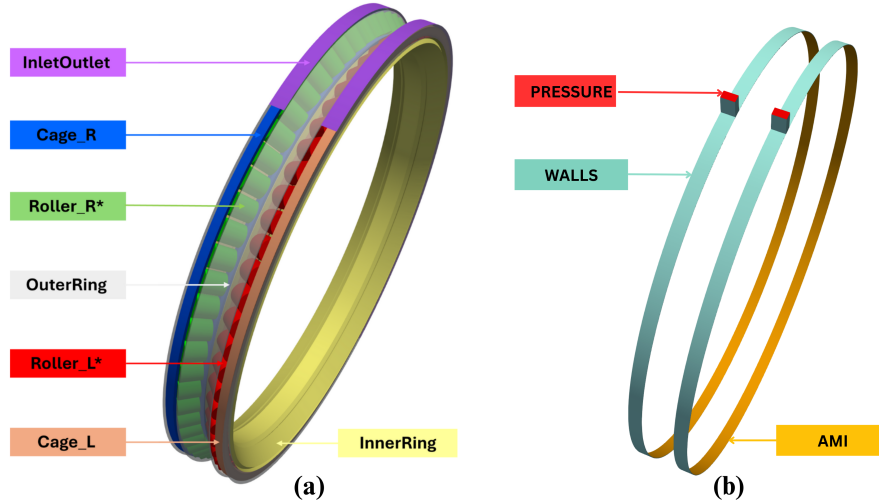
Figure 5. (a) Patches corresponding to bearing components **(b)** Additional patches defined for imposing pressure BCs

measure of how much the cell deviates from ideal shape. A value of more than 4 creates numerical errors during simulation. Non-orthogonality is the measure of angle between the normal of face and vector connecting the center of neighbouring cell. If the maximum non-orthogonality is more than $70°$, it will cause instability in simulation. The face volume ratio is the measure of the difference of volumes of adjacent cells. Abrupt changes in the volume of cells in the mesh leads to numerical errors. The

155   value close to 1 shows an excellent mesh quality. The mesh developed for bearing, all these values were in acceptable range as witnessed from Table 2.

2.3 Governing Equations

2.3.1 CFD Governing Equations

Two fundamental laws of conservation were solved in this study i.e. law of conservation of mas (Continuity equation) and

160   law of conservation momentum (Navier-Stokes equation). The fluid domain was considered as isothermal, therefore, energy equation was not solved in the model. Continuity equation for incompressible flow is shown as Eq. 5 and in expanded form in Eq. 6.

$$\nabla \cdot \mathbf{u} = 0 \tag{5}$$

$$\frac{\partial u}{\partial x} + \frac{\partial v}{\partial y} + \frac{\partial w}{\partial z} = 0 \tag{6}$$

165   where $\mathbf{u}$ is the velocity vector. Navier-Stokes equation for incompressible and non-Newtonian fluid is shown as Eq. 7

Table 2. Key parameters of mesh quality

Parameter	Value
Points	13891995
Faces	38814880
Internal Faces	35907560
Roller Faces (each)	6864
Cage Faces (each)	400010
Inner Raceway Faces	629460
Outer Raceway Faces	464880
InletOulet Faces	120640
Cells	12453740
Max Cell Openness	5.34177e-16
Max Aspect Ratio	13.968
Max Skewness	2.37913
Average Non-orthogonality	24.1692
Average Face Volume Ratio	0.926

$$\rho \left(\frac{\partial \mathbf{u}}{\partial t} + (\mathbf{u} \cdot \nabla)\mathbf{u} \right) = -\nabla p + \nabla \cdot \boldsymbol{\tau} + \rho \mathbf{g} + \mathbf{F} \tag{7}$$

where ρ is the fluid density, $\mathbf{u}$ is the velocity vector, $\boldsymbol{\tau}$ is the stress tensor (includes pressure and viscous stress), $\rho \mathbf{g}$ represents body forces like gravity, $\mathbf{F}$ includes additional external forces.

2.3.2 Volume of Fluid Model

170 The fluid domain studied in this study was grease and air. Volume of Fluid (VoF) model was used to capture interface between these two immiscible fluid phases. This model is useful for multiphase simulation ensuring smooth transition of different properties across the interface. The volume fraction of grease and air must be equal to 1 satisfying the balance Eq. 8.

$$\alpha_{\text{grease}} + \alpha_{\text{air}} = 1 \tag{8}$$

where α_{grease} is volume fraction of grease and α_{air} is volume fraction of air. If the fluid in cell is only grease, then α_{grease} is

175 equal to 1, and if it is only air, then α_{grease} is equal to 0. The weighted average equation in the VoF method for density is given by:

$$\rho_{\text{avg}} = \alpha_{\text{grease}} \cdot \rho_{\text{grease}} + (1 - \alpha_{\text{grease}}) \cdot \rho_{\text{air}} \tag{9}$$

Other properties can be calculated using a similar approach.

2.3.3 Kinematics of TRB

180 The kinematics of key components i.e., rollers, cage, inner, and outer raceways play important role in the CFD modelling of TRB. In kinematics of TRB, cone angle (α), roller mean diameter (d_R), pitch radius ($D_p/2$), and rotational directions of shaft speed (ω_S), roller speed (ω_R), and cage speed (ω_C) play significant role.

Cone angle (α) is the angle between the bearing axis and roller axis. In TRBs, all the rollers axes intersect the bearing axis at one common point. This point is called apex point. For double-row TRB, two apex points opposite to each other are present,

185 each for its respective row. This design ensures the pure rolling motion of rollers, and uniform distribution of radial and axial loads. Equations 10 and 11 show that the rotational speed of cage (ω_C) and rollers (ω_R) can be expressed in terms of these geometric parameters (d_R, D_p, and α) and shaft rotational speed ω_S (Maccioni et al., 2023a).

$$\omega_{\mathrm{C}} = \omega_{\mathrm{S}} \cdot \frac{1}{2}\left(1 - \frac{d_{\mathrm{R}}}{D_{\mathrm{p}}}\cos\alpha\right) \tag{10}$$

190 $$\omega_{\mathrm{R}} = \omega_{\mathrm{S}} \cdot \frac{1}{2}\left\{\frac{D_{\mathrm{p}}}{d_{\mathrm{R}}}\left[1 - \left(\frac{d_{\mathrm{R}}}{D_{\mathrm{p}}}\cos\alpha\right)^2\right]\right\} \tag{11}$$

ω_S is considered the input velocity. Inner raceway rotates with the same velocity as ω_S while the outer raceway is stationary.

2.3.4 Lubrication Model

In this study, grease is used as a lubricant. Grease is a non-Newtonian fluid exhibiting complex behaviour under varying shear rates. At low shear rates, the viscosity of grease is high and behaves as solid upto its yield point. At high shear rates, viscosity

195 decreases and grease manages to flow. This behaviour is called shear thinning. This behaviour can be witnessed from the experimental data for the grease used in this study as shown in Fig. 6a.

Herschel-Bulkley model was used to accurately describe this complex rheological behaviour of grease. This model is represented as Eq. 12;

$$\tau = \tau_y + K\dot{\gamma}^n \tag{12}$$

200 where τ is the shear stress, τ_y is the yield stress, K is the consistency index, $\dot{\gamma}$ is the shear rate, n is the flow behaviour index. τ_y, K, and n were determined from experimental data using the concept of curve fitting. MATLAB® script was developed in which sum of squared errors method was implemented to calculate these parameters. Experimental data and calculated data were in strong agreement with each other as shown in Fig. 6b.

Some important physical properties of the grease used in this study are listed in Table 3.

(a)   **(b)**
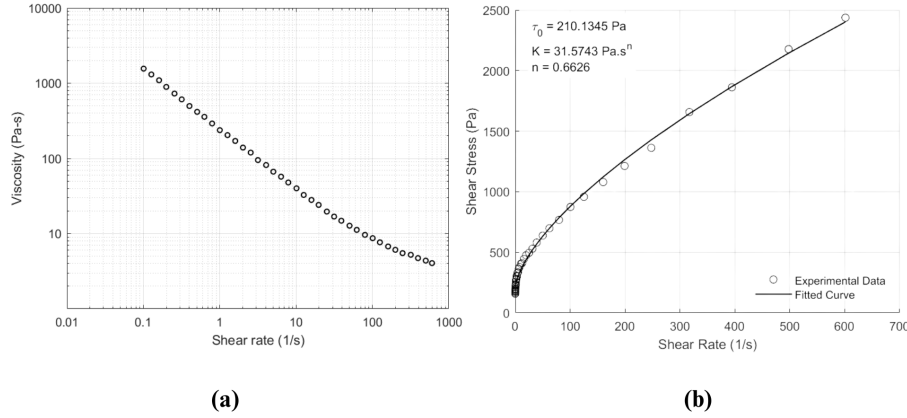
Figure 6. Illustrating shear thinning behaviour of the grease (at 25 °C) used in this study **(a)** Experimental data **(b)** Curve-fitted data

Table 3. Properties of grease at 25 °C

Property	Unit	Value
Density	$\mathrm{kgm^{-3}}$	930
Kinematic viscosity	$\mathrm{m^2 s^{-1}}$	0.0016
Yield Stress	Pa	210.1345
Consistency index	$\mathrm{Pas^n}$	31.5743
Flow index (n)	-	0.6626
NLGI grade	-	1

2.4 Boundary Conditions (BCs)

The interaction of fluid with the boundaries of domain in CFD analysis is defined by BCs. Therefore, appropriated BCs play significant role in accurately replicating the physical conditions in CFD environment. In this paper, the most appropriate BCs for velocity, relative pressure, and grease volume fraction were applied to respective patches as shown in Table 4.

Rigid Mesh Motion (RMM) model was implemented to ensure the mesh rotation around bearing axis as single, unde-formable entity. In our case, the mesh rotational speed was set to the same rotational speed as that of the cage. Therefore, movingWallVelocity BC was applied to cage to ensure zero relative velocity (no slip) between walls of cage and mesh. The rotatingWallVelocity BC was applied to inner ring and outer ring. Inner ring was rotated around a fixed axis (bearing axis) with the same rotational speed as that of shaft, whereas, outer ring was set as stationary. The conical rollers exhibit combined motion i.e., spinning about their own axis (dynamic axis) and rotating around bearing axis (fixed axis). To replicate this complex

Table 4. Boundary Conditions (BCs) applied

Patch	U[m/s]	p[Pa]	p_rgh[Pa]	α[-]
RollerL[1-65]	conicalWallVelocity	zeroGradient	zeroGradient	zeroGradient
RollerR[1-65]	conicalWallVelocity	zeroGradient	zeroGradient	zeroGradient
InnerRing	rotatingWallVelocity	zeroGradient	zeroGradient	zeroGradient
OuterRing	rotatingWallVelocity	zeroGradient	zeroGradient	zeroGradient
Cage_L	movingWallVelocity	zeroGradient	zeroGradient	zeroGradient
Cage_R	movingWallVelocity	zeroGradient	zeroGradient	zeroGradient
InletOutlet	cyclicAMI	cyclicAMI	cyclicAMI	cyclicAMI
AMI	cyclicAMI	cyclicAMI	cyclicAMI	cyclicAMI
PRESSURE	zeroGradient	fixedValue	fixedValue	inletOutlet
WALLS	fixedValue	zeroGradient	zeroGradient	zeroGradient

215 combination of motion, a new custom BC, named conicalWallVelocity was applied to each roller, as their own axes of rotation were unique. The zeroGradient BCs corresponded to the conditions where the respective variables were not changing in perpendicular direction to the boundary faces. Non-conformal faces with different mesh structures were connected via cyclicAMI (Arbitrary Mesh Interface) BC. Gravitational effects are significant and are taken into account in this study. Since the bearing is tilted, the components of gravitational acceleration are resolved accordingly and applied to the bearing.

220 2.5 Solver Setup

In this study, the case was considered as multiphase, incompressible, laminar, and isothermal. The most appropriate solver available in OpenFOAM is interFoam for solving these conditions. This solver use VoF model to solve multiphase flows. Therefore, it was used in our study. The numerical stability, convergence, and good simulation speed were ensured by limiting the Courant number (Co) to less than 1. First order implicit Euler scheme was used for time discretization, whereas Gauss
225 theorem was used for gradient calculation.

3 Simulated Operating Conditions

In this study, the grease filling ratio within the bearing was varied, keeping the rotational speed and other conditions the same. These operating conditions are listed in Table 5. Simulations were performed for one full rotation of the cage utilizing 24 cores of a High-Performance Computing (HPC) cluster.

Table 5. Simulated operating conditions

Simulation	Shaft rotational speed (rpm)	Grease filling ratio
1	17.5	45 %
2	17.5	35 %
3	17.5	21 %

4   Results and Discussion

4.1   Grease Distribution

In this study, the grease filling ratios were kept below 50% of the total volume of the bearing's lubricating chamber to better represent critical operating conditions. The total volume of bearing's lubricating chamber is 0.0347001 m^3. Figure 7 depicts the respective grease filling ratios for the three simulations. Simulation 3 employs the lowest filling ratio—21 % of the total volume (Fig. 7c)—which represents the most critical condition. It shows the initial grease level positioned just below the outlet ports within the lubricating chamber.
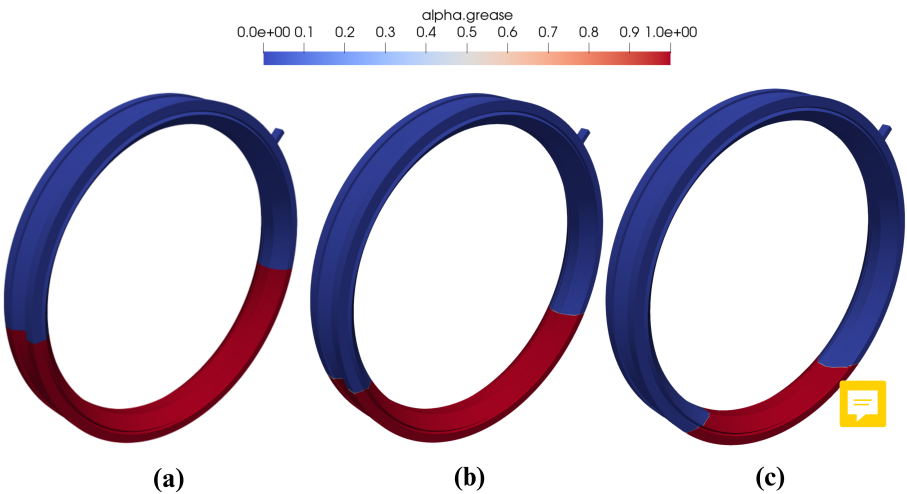
Figure 7. Grease filling ratios **(a)** 45 % **(b)** 35 % **(c)** 21 % of the total volume of bearing's lubricating chamber (images were captured as viewed from MFS)

The grease distribution inside the bearing after one complete rotation of bearing is shown in Fig. 8. As observed in Fig. 8, the upper region of the bearing exhibits signs of grease starvation, with noticeably less lubricant compared to the lower region for all the three grease filling ratios. This phenomenon is attributed to the influence of gravity.

(a) **(b)** **(c)**
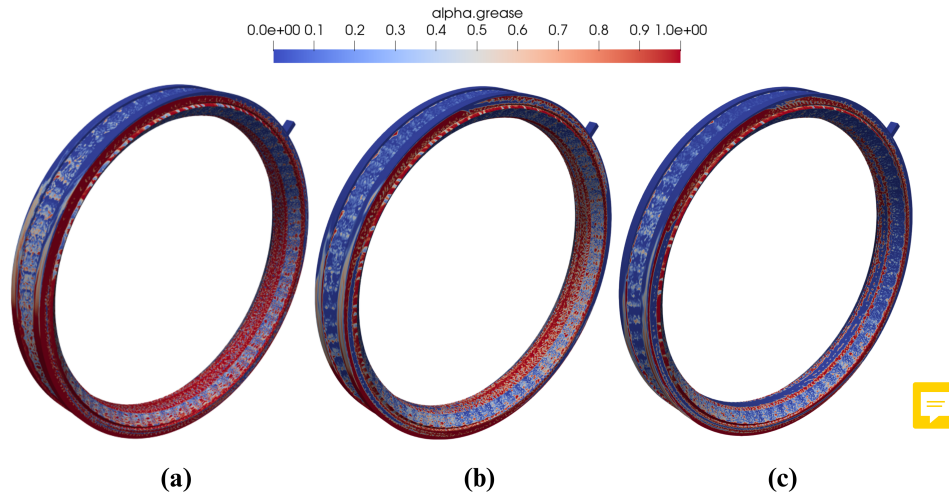
Figure 8. Grease distribution after one rotation of cage **(a)** 45 % **(b)** 35 % **(c)** 21 % grease filling ratios

240   The disparity in grease distribution is further illustrated in Fig. 9, which provides a clearer comparison between the top and bottom sections for the three simulations. For 45 % grease filling ratio (Fig. 9a), the wetted volume of the upper part of the bearing is $0.004365 \, \mathrm{m}^3$, whereas the lower part has a wetted volume of $0.01148 \, \mathrm{m}^3$ — approximately 41 % greater than that of the upper region. For 35 % grease filling ratio (Fig. 9b), the wetted volume of the upper part of the bearing is $0.00311593 \, \mathrm{m}^3$, whereas the lower part has a wetted volume of $0.00885667 \, \mathrm{m}^3$ — approximately 36 % greater than that of the upper region.

245   For 21 % grease filling ratio (Fig. 9c), the wetted volume of the upper part of the bearing is $0.00133971 \, \mathrm{m}^3$, whereas the lower part has a wetted volume of $0.00575628 \, \mathrm{m}^3$ — approximately 25.6 % greater than that of the upper region.

The tilt of the bearing also influences the grease distribution behavior. To analyze this effect, the two rows of the bearing were separated, and the corresponding grease distribution was captured for each filling ratio as shown in Fig. 10. The total volume of the lubrication chamber for each row is $0.0174 \, \mathrm{m}^3$. After one complete rotation of cage, the wetted volume in

250   the MFS row is $0.008645 \, \mathrm{m}^3$, whereas the hub side (HS) row has a wetted volume of $0.007203 \, \mathrm{m}^3$ for 45 % grease filling ratio. This indicates that the MFS row retains approximately 8.5 % more grease than the HS row. For 35 % ratio, the wetted volume in the MFS row is $0.00667421 \, \mathrm{m}^3$, whereas the hub side (HS) row has a wetted volume of $0.00530031 \, \mathrm{m}^3$ indicating approximately 7.9 % more grease in the MFS row. Similarly for 21 % grease filling ratio, the difference between the wetted volume in MFS and HS row is 6.35 %.

255   Figure 11 illustrates the asymmetric distribution of grease over time. Initially, both rows exhibit equal grease occupancy. However, once rotation begins, the grease volume in the MFS row (i.e., the row toward which the bearing is tilted) gradually increases, accompanied by a corresponding decrease in the HS row. This behavior can be attributed to the influence of centrifugal forces, which drive the grease radially outward. Due to the bearing tilt, this outward flow is biased toward the MFS row, resulting in a pressure build-up in that region. An interesting phenomenon of grease redistribution begins to occur after
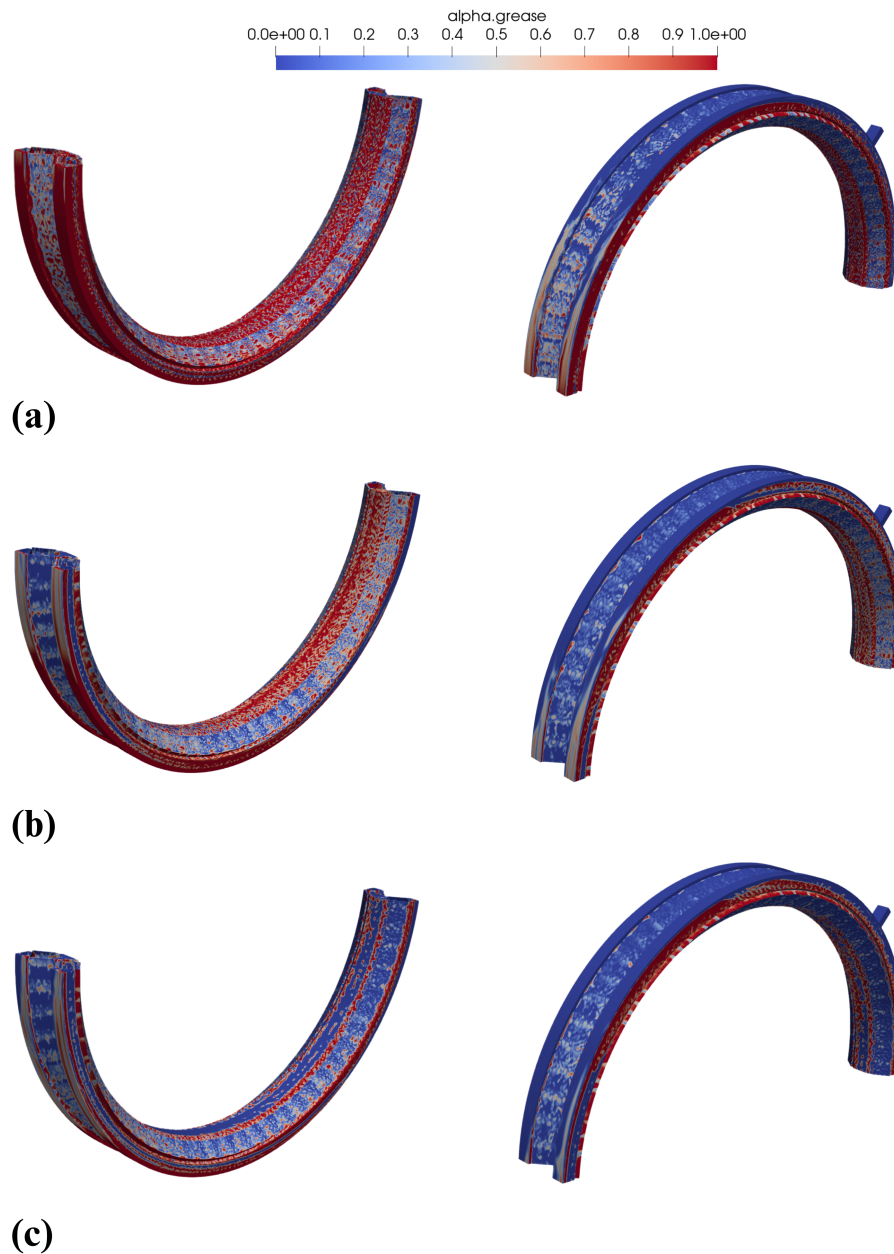
Figure 9. Illustration of comparison of grease distribution in top and bottom part of the bearing after one rotation of cage **(a)** 45 % **(b)** 35 % **(c)** 21 % grease filling ratios

260 certain period of time. As the pressure in the MFS row increases, a sufficient pressure gradient is established between the two rows. This gradient drives the grease back toward the HS row, counteracting the centrifugal bias. Eventually, a steady state is
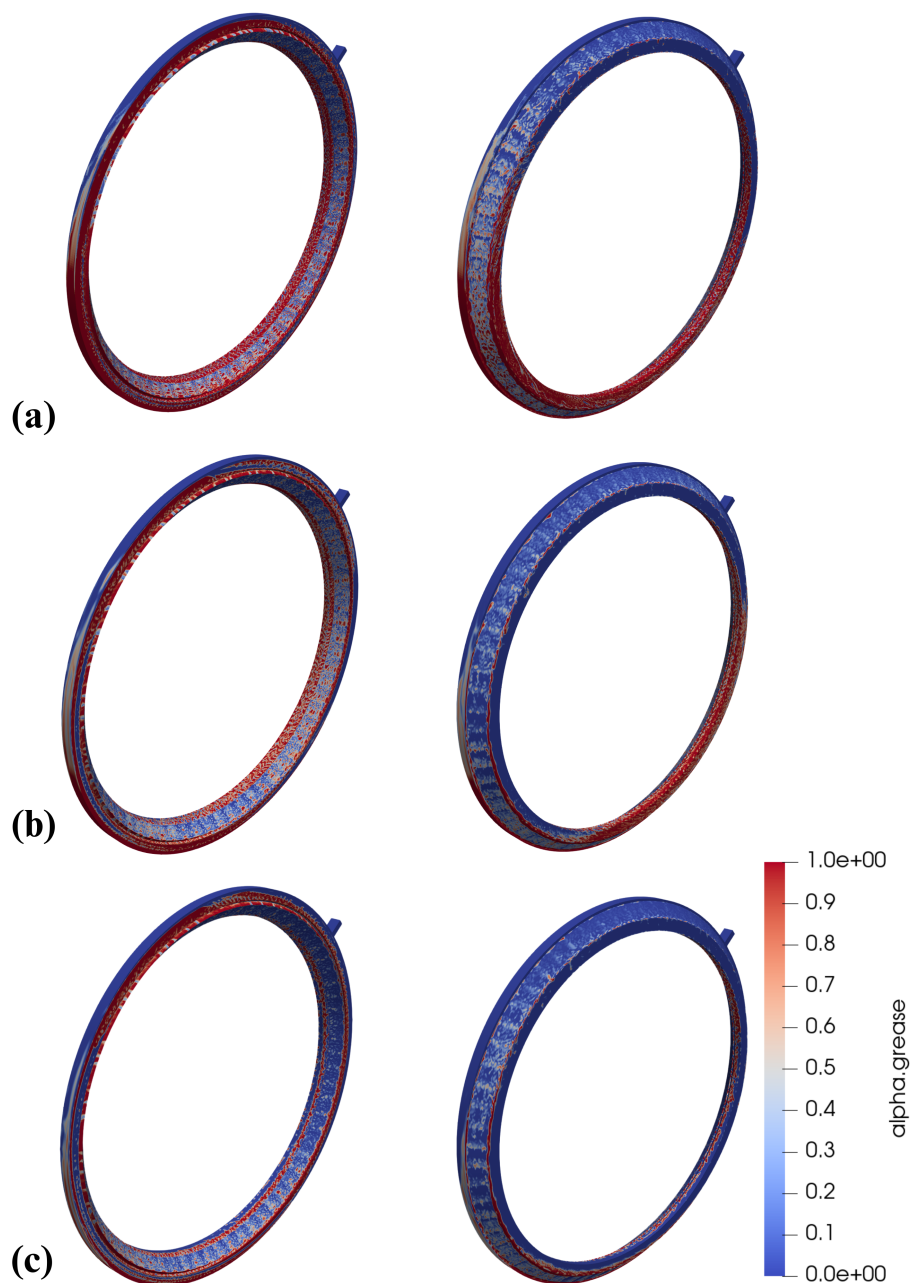
Figure 10. Illustration of grease distribution in MFS and HS row after one rotation of cage **(a)** 45 % **(b)** 35 % **(c)** 21 % grease filling ratios

reached in which a dynamic equilibrium exists between the centrifugal-driven flow and the pressure-induced backflow. At this stage, the net grease flow between the rows becomes negligible and the grease distribution stabilzes.
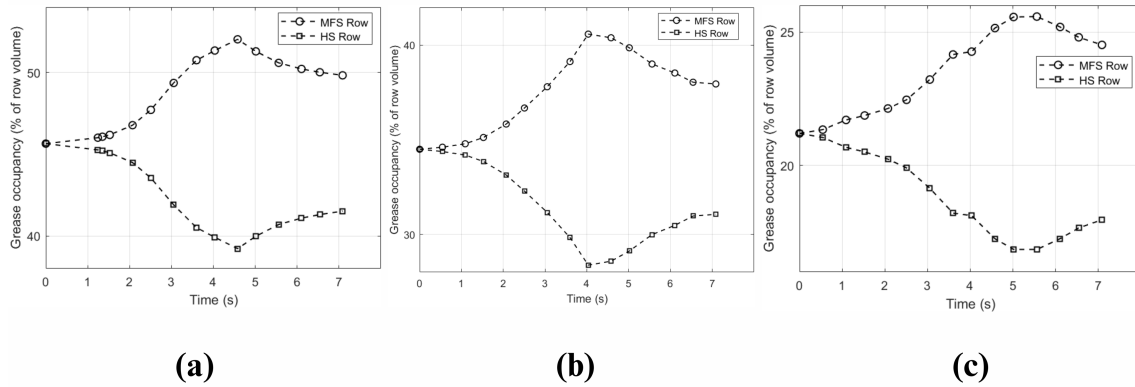
Figure 11. Illustration of asymmetrical grease occupancy as a percentage of lubrication chamber volume of each row w.r.t time **(a)** 45 % **(b)** 35 % **(c)** 21 % grease filling ratio

Figure 12 illustrates the temporal evolution of the grease film angle (θ) for three different grease filling ratios. The angles
265 are measured with respect to the bottommost part of the bearing (i.e., $\theta = 0°$), and represent the extent to which the grease progresses toward the topmost region ($\theta = 180°$) under rotation. The initial grease levels in the rotating direction (positive x-axis) are approximately $82°$, $62°$, and $36°$ for the 45 %, 35 %, and 21 % filling ratios, respectively. These values reflect the initial angular spread of the grease before rotation begins.

Figure 12a presents the grease film evolution on the MFS inner raceway. It is evident that, for all three filling ratios, the
270 grease film progresses up to the topmost region of the bearing. However, the time required to reach this position varies with the filling ratio, with higher ratios achieving full coverage more rapidly. The corresponding distribution on the HS inner raceway is shown in Fig. 12b. In this case, the 45 % and 35 % filling ratios allow the grease film to reach the top region, similar to the MFS side. However, for the 21 % filling ratio, the grease front diminishes significantly and fails to reach the upper portion, indicating a thinning film and potentially inadequate lubrication in this area.

275 Figure 12c shows the grease progression on the MFS outer raceway. Only the 45 % filling ratio provides sufficient grease volume to reach the topmost section. For the 35 % and 21 % cases, the upper region remains starved. This behavior can be attributed to the fact that the outer raceway is stationary and, therefore, does not contribute to the centrifugal transport of grease. As a result, the grease tends to remain with the rotating inner raceway and rollers, limiting its migration toward the outer raceway—especially under low grease volumes. Finally, Figure 12d illustrates the HS outer raceway. In this case, none
280 of the three filling ratios succeed in delivering grease to the top region, leaving it starved throughout the simulation. This consistent starvation across all cases emphasizes the asymmetric grease distribution resulting from the bearing's tilt and the centrifugal-biased flow towards the MFS side.

It is important to note that in cases where the grease fails to reach the topmost region, the limited amount of grease causes the front to gradually disappear over time. After a certain point, the grease becomes too sparse to form a continuous layer, instead

285 breaking into small dispersed droplets. As a result, it is not possible to extract a well-defined angle of progression beyond this stage. Therefore, data beyond this point were excluded from the graph, as no coherent front exists to track angular progression reliably.
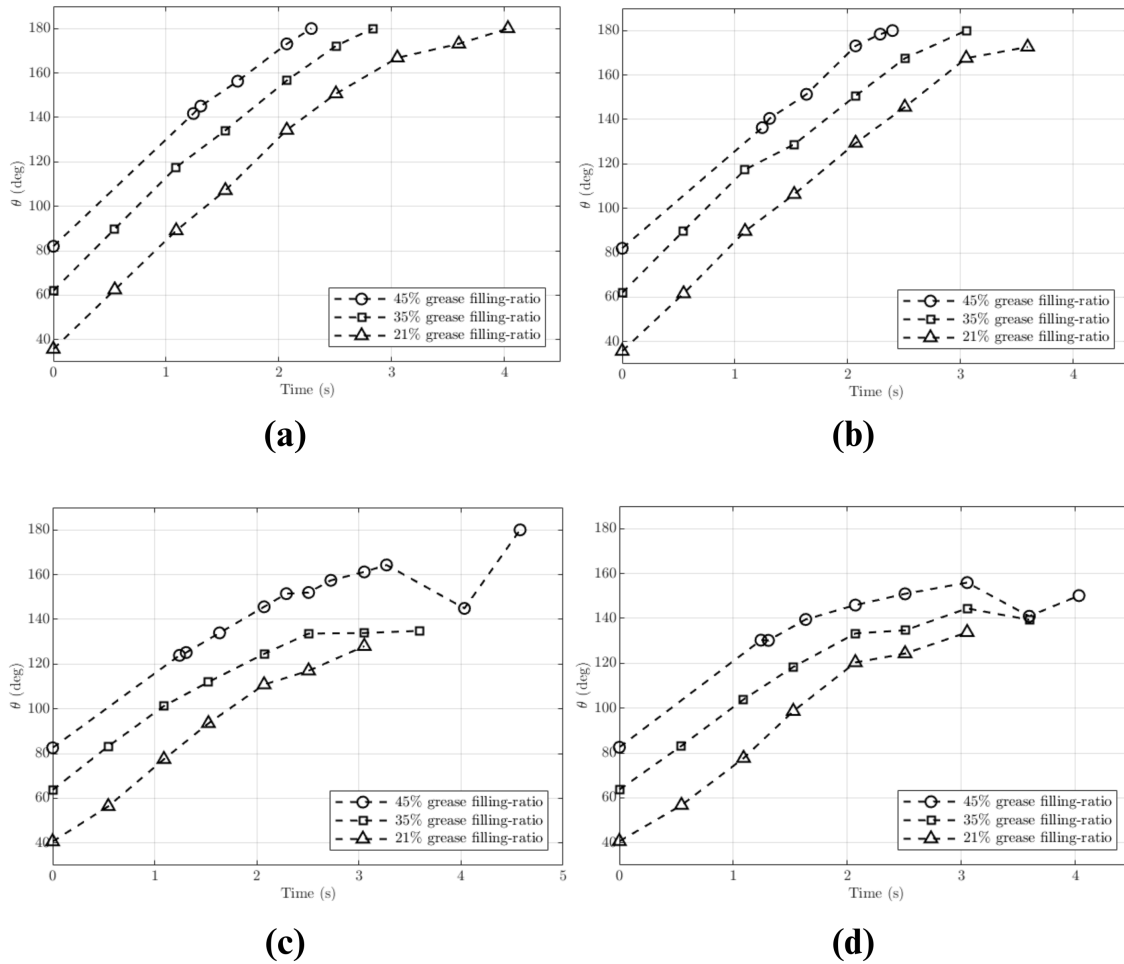
Figure 12. Illustration of the temporal distribution of the grease within the range of $0° \leq \theta \leq 180°$ **(a)** MFS inner raceway **(b)** HS inner raceway **(c)** MFS outer raceway **(d)** HS outer raceway

4.2 Fluxes

Figures 13 and 14 illustrate the velocity fields in cross-sectional slices taken from planes perpendicular to the bearing axis for
290 the MFS and HS rows, respectively. It is evident that the velocity of the fluid varies between the speeds of the cage and the rollers throughout the domain, except in regions adjacent to the inner and outer raceways, where the fluid adheres to the no-slip

boundary condition. Additionally, higher fluid velocities are observed near the roller surfaces, emphasizing the critical role of the rollers in promoting fluid motion within the bearing.
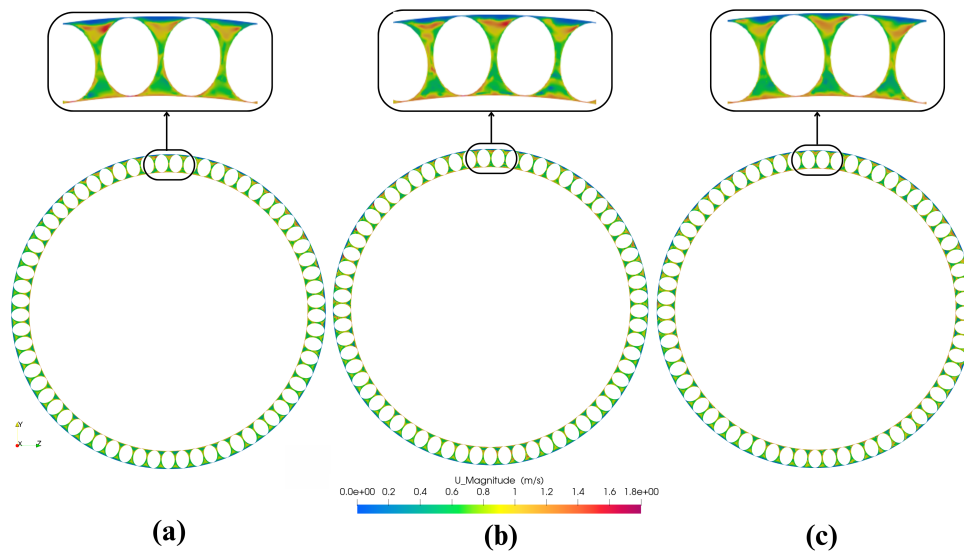
Figure 13. Illustration of velocity fields in MFS row after one rotation of cage **(a)** 45 % **(b)** 35 % **(c)** 21 % grease filling ratio
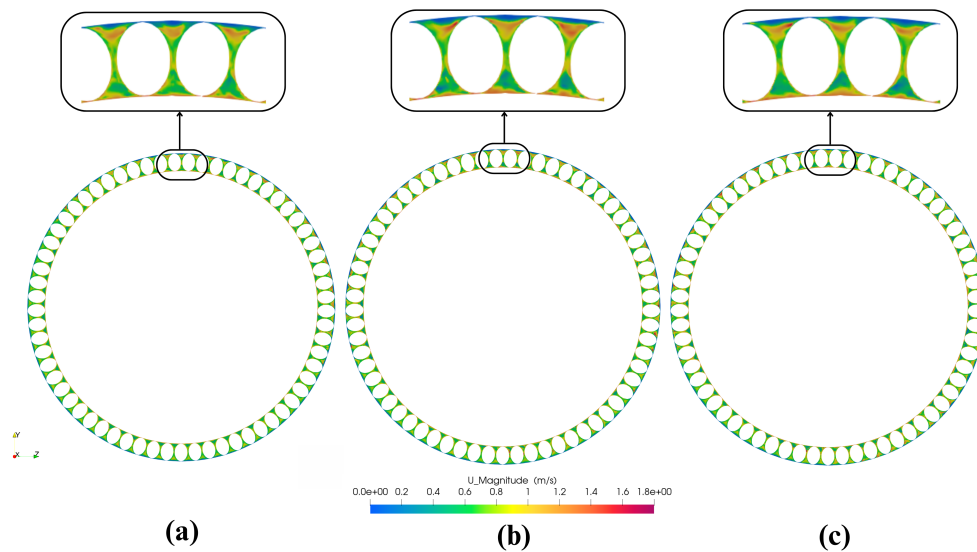
Figure 14. Illustration of velocity fields in HS row after one rotation of cage **(a)** 45 % **(b)** 35 % **(c)** 21 % grease filling ratio

The pumping effect induced by the rollers, resulting from their tapered geometry, is illustrated in Figs. 15 and 16 corresponding to the MFS and HS rows, respectively. Due to this geometry, one side of each roller exhibits outward axial velocity,

295

while the opposite side shows inward axial velocity. This asymmetric velocity distribution contributes to the axial transport of lubricant within the bearing. Specifically, on the MFS side, negative axial velocity indicates outward flow, whereas on the HS side, it corresponds to inward flow. Conversely, positive axial velocity represents inward flow on the MFS side and outward flow on the HS side. This bidirectional flow pattern highlights the role of tapered rollers in driving lubricant circulation across the bearing rows.
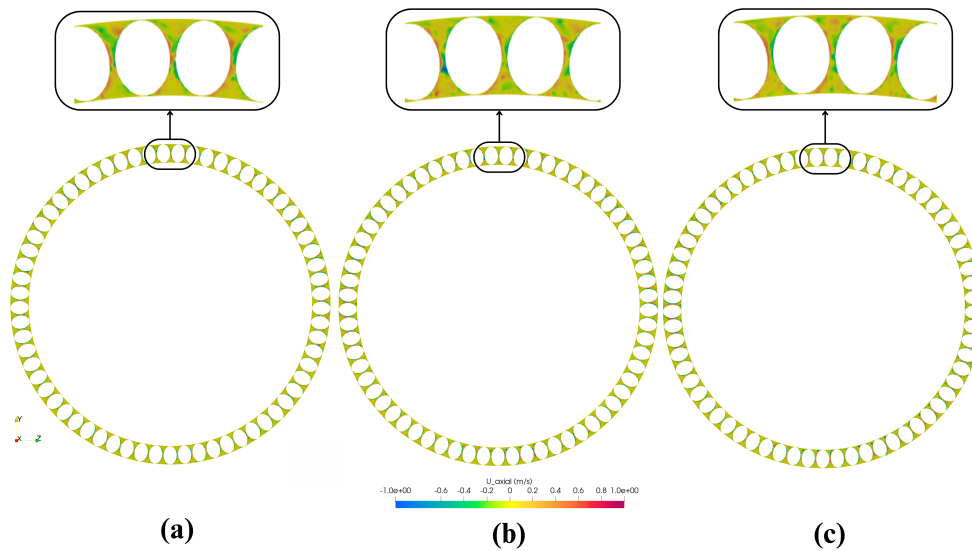
Figure 15. Illustration of axial velocity fields in MFS row after one rotation of cage **(a)** 45 % **(b)** 35 % **(c)** 21 % grease filling ratio

4.3 Pressure Fields

The pressure field developed due to grease flow over the roller surfaces and inner raceway is illustrated in Fig. 17. Higher pressure regions are observed in areas with greater lubricant accumulation which is evident from Fig. 17a that for 45 % grease filling ratio, the pressure developed inside the bearing is higher as compared to 35 % and 21 % filling ratios (Figs. 17b and 17c). Notably, steep pressure gradients occur near the contact interfaces between the rollers and raceways, which can be attributed to the squeezing effect of the lubricant in these narrow gaps. Similar pressure trends were found by Maccioni et al. (2023a) in their study.

The pressure distribution on the bearing seals is of particular importance, as it directly affects the potential of lubricant leakage. Figure 18 presents the pressure profiles on both the MFS and HS seals for the three grease filling ratios. The left column corresponds to the MFS seal, while the right column shows the HS seal. It is evident that the pressure on the seals is highest for the 45 % grease filling ratio, followed by 35 % and 21 %, indicating that increased grease volume leads to greater sealing pressure and potentially a higher risk of leakage.
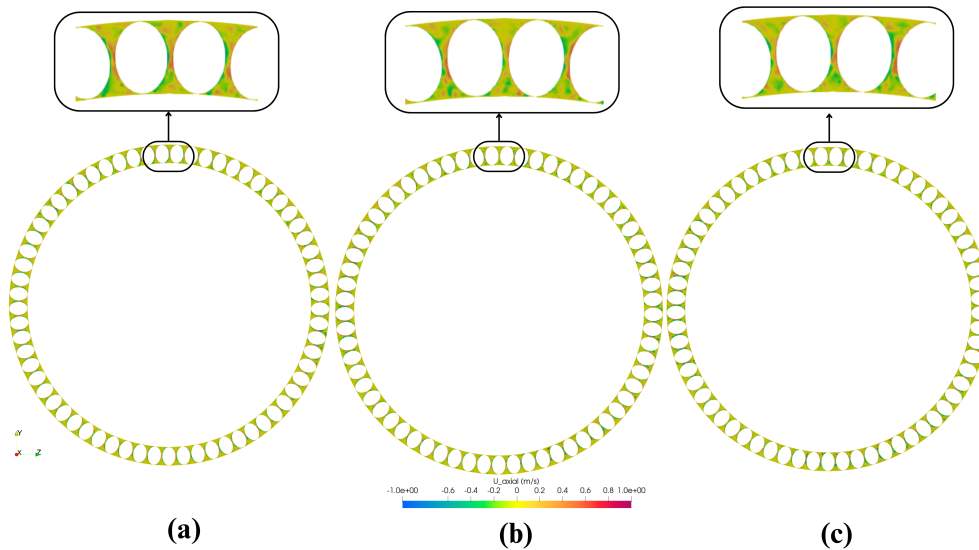
Figure 16. Illustration of axial velocity fields in HS row after one rotation of cage **(a)** 45 % **(b)** 35 % **(c)** 21 % grease filling ratio

4.4 Grease Settling Behaviour

To gain further insight in understanding the behavior of grease within the bearing, further study was conducted to evaluate the time required for the grease to settle after the bearing rotation stops. The simulation was carried out for operating conditions i.e. 45 % filling ratio, 0 rpm, and a temperature of 40 °C.

The grease distribution after one complete rotation of cage was taken from the results of simulation 1. At this point, the bearing was brought to a stop (0 rpm), and the grease temperature was maintained at 40 °C. The system was then monitored to observe the redistribution of grease as it gradually settled back toward its pre-rotation state. These operating conditions were designed to replicate a real-world scenario, such as a wind turbine shutdown, to assess how long it would take for the grease to migrate back to the lower region of the bearing under gravity-driven effects. The grease distribution across the top and bottom sections of the bearing after 40 seconds is illustrated in Fig. 19, and the temporal evolution of the settling process is presented in Fig. 20. It is observed that approximately 98 % of the grease volume settled back to the lower region of the bearing within 40 seconds.
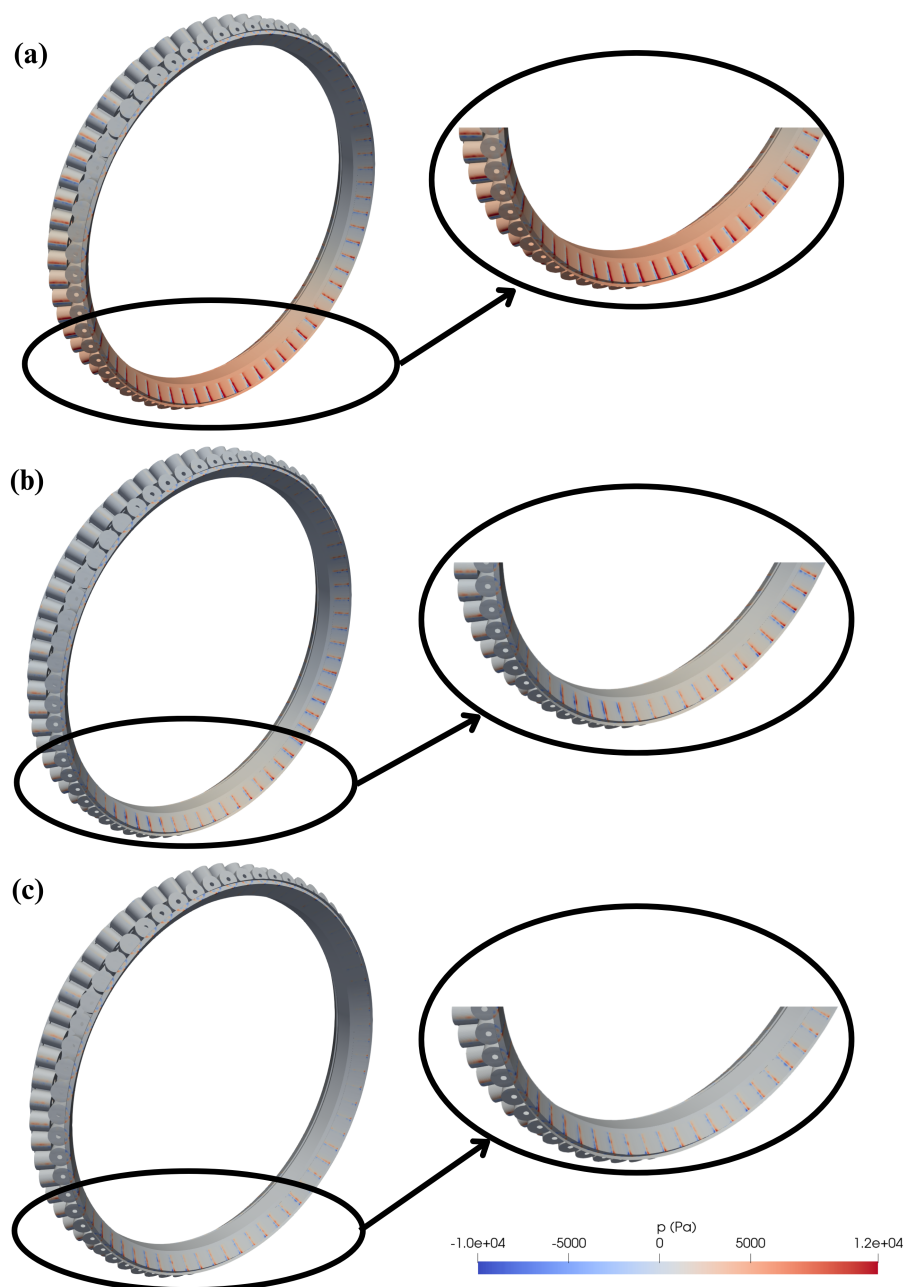
Figure 17. Illustration of pressure fields in rollers and inner raceway after one rotation of cage (steep pressure gradients near the contact surfaces) **(a)** 45 % **(b)** 35 % **(c)** 21 % grease filling ratio
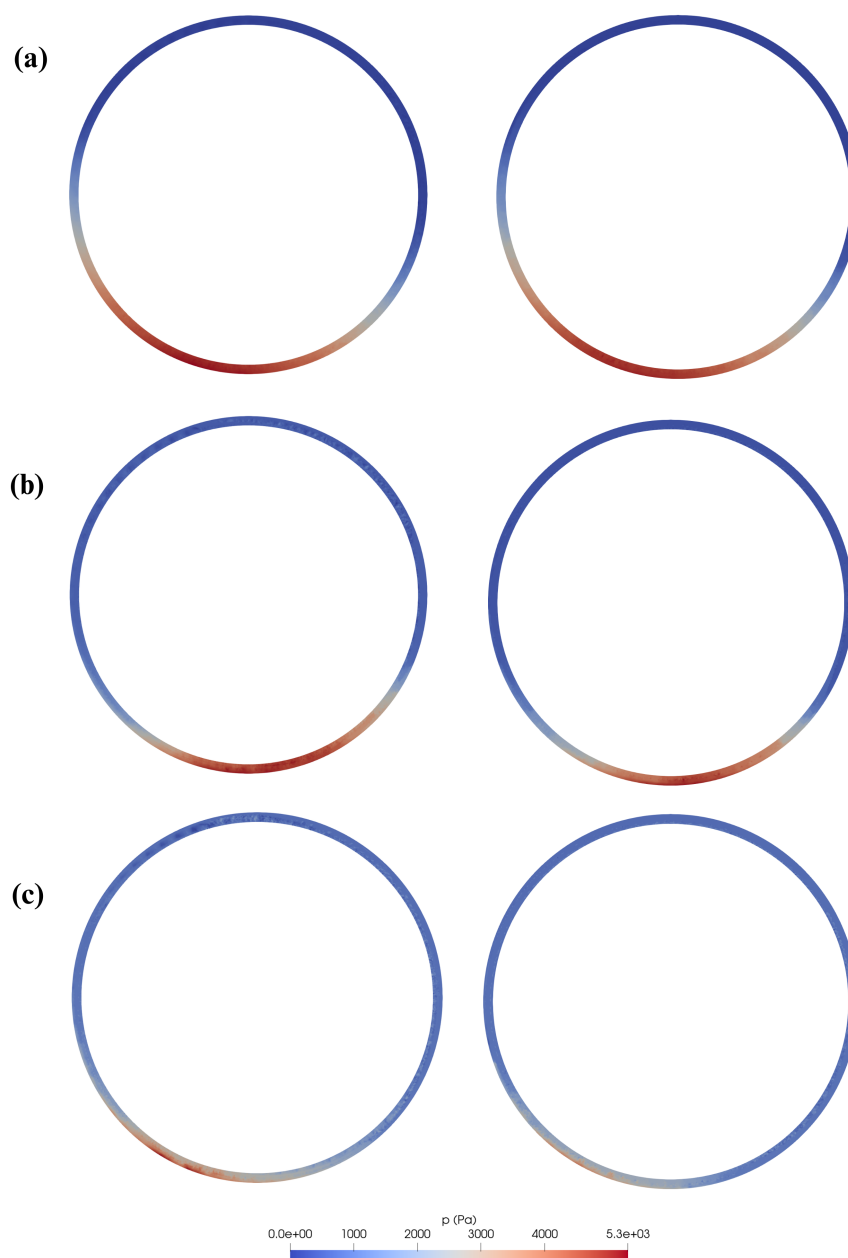
Figure 18. Illustration of pressure fields in MFS and HS seals after one rotation of cage **(a)** 45 % **(b)** 35 % **(c)** 21 % grease filling ratio
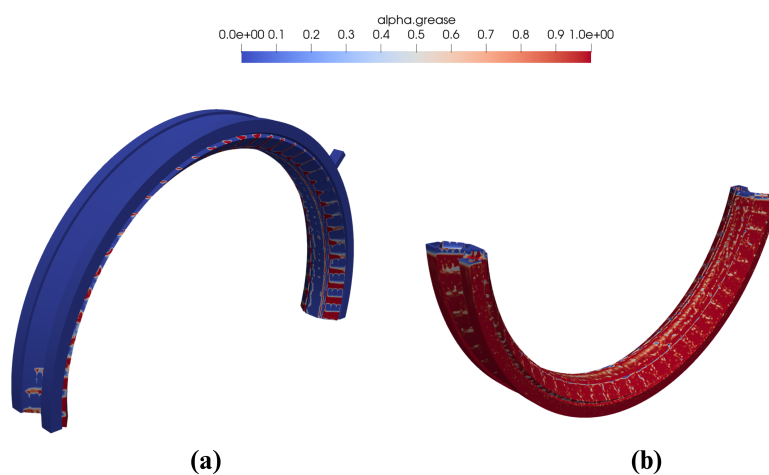
Figure 19. Illustration of grease settling behaviour for 45 % filling ratio at 40 °C **(a)** top part **(b)** bottom part
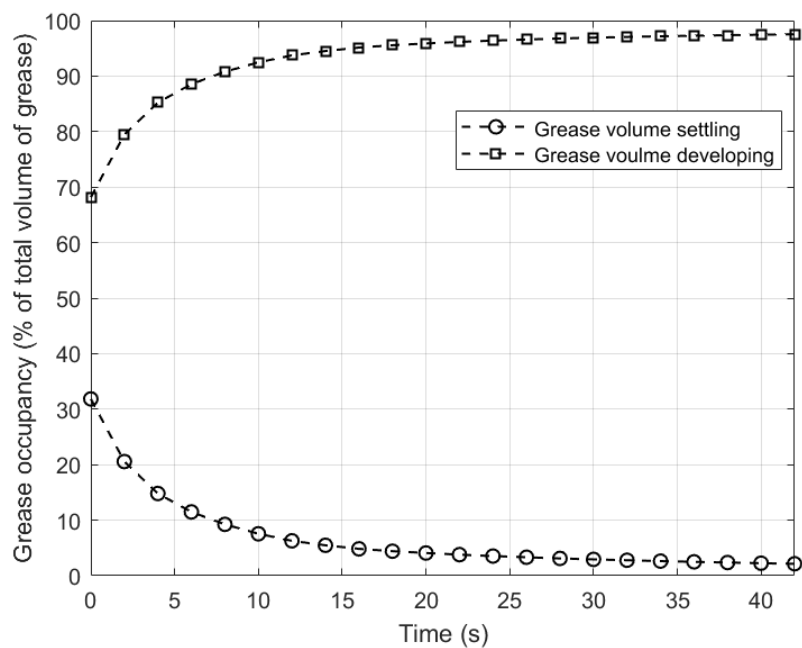
Figure 20. Illustration of grease settling behaviour for 45 % filling ratio at 40 °C w.r.t time

5 Conclusions

The primary objective of this study was to develop a full-scale CFD model of a tilted 41513219 double-row TRB to analyze the behavior of a non-Newtonian lubricant—specifically, grease—under various operating conditions. An extensive three-dimensional hexahedral mesh of the entire bearing geometry was generated in OpenFOAM® using a parametric approach implemented through a custom MATLAB® script. The final mesh comprised approximately 12.5 million cells. A VoF model was employed to accurately capture the interface between grease and air. The complex rheological characteristics of the grease were modeled using the Herschel–Bulkley formulation.

The developed CFD model provided in detail the key lubrication characteristics by simulating the bearing behavior at three grease filling ratios. Using this model, detailed analyses of grease distribution, pressure fields, and velocity profiles were conducted. Lubricant behavior within the bearing is significantly influenced by gravitational and tilting effects. The upper region of the bearing exhibits noticeable grease starvation compared to the lower region due to gravitational settling. Additionally, the tilt toward the main MFS results in greater grease accumulation in the MFS row relative to the HS row.

In this study, simulations were conducted for varying grease filling ratios. The developed model can also be extended to simulate different operating conditions, such as variations in rotational speed and grease rheological properties. Overall, the developed model provides a robust framework for analyzing lubrication behavior in large-scale double-row tapered roller bearings and serves as a valuable tool for optimizing lubrication system design. A state of the art test rig is in the developing stage which will further enhance the depth of understanding regarding lubrication physics involved in double-row TRBs in large sizes.

Author contributions. Conceptualization, M.I.K., L.M., F.C.; methodology, M.I.K.; software, M.I.K., L.M.; validation, M.I.K.; formal analysis, M.I.K.; investigation, M.I.K.; resources, F.C.; data curation, M.I.K.; writing—original draft preparation, M.I.K.; writing—review and editing, M.I.K., L.M., F.C.; visualization, M.I.K.; supervision, L.M., F.C.; project administration, F.C.; funding acquisition, F.C. All authors have read and agreed to the published version of the manuscript.

Competing interests. The authors declare that they have no conflict of interest.

Financial support. This research was funded by PNRR DM117 I52B23000570003.

References

350 Aamer, S., Sadeghi, F., Russell, T., Peterson, W., Meinel, A., and Grillenberger, H.: Lubrication, flow visualization, and multiphase CFD modeling of ball bearing cage, Tribology Transactions, 65, 1088–1098, 2022.

Bercea, I., Cretu, S., and Nélias, D.: Analysis of double-row tapered roller bearings, Part I-Model, Tribology transactions, 46, 228–239, 2003.

Chen, H., Liang, H., Wang, W., and Zhang, S.: Investigation on the oil transfer behaviors and the air-oil interfacial flow patterns in a ball bearing under different capillary conditions, Friction, 11, 228–245, 2023.

355 Concli, F., Schaefer, C. T., and Bohnert, C.: Innovative meshing strategies for bearing lubrication simulations, Lubricants, 8, 46, 2020.

Crouchez-Pillot, A. and Morvan, H. P.: CFD simulation of an aeroengine bearing chamber using an enhanced volume of fluid (VOF) method: An evaluation using adaptive meshing, in: Turbo Expo: Power for Land, Sea, and Air, vol. 45738, p. V05CT16A033, American Society of Mechanical Engineers, 2014.

Deng, S., Zhao, G., Qian, D., Jiang, S., and Hua, L.: Investigation of oil–air flow and temperature for high-speed ball bearings by combining
360 nonlinear dynamic and computational fluid dynamics models, Journal of Tribology, 144, 071 204, 2022.

Feldermann, A., Fischer, D., Neumann, S., and Jacobs, G.: Determination of hydraulic losses in radial cylindrical roller bearings using CFD simulations, Tribology International, 113, 245–251, 2017.

Gao, P., Tang, W., Cui, Y., Wang, Y., Mo, G., and Yin, J.: Theoretical and Experimental Investigation on Thermal Characteristics of Railway Double-Row Tapered Roller Bearing, Energies, 15, https://doi.org/10.3390/en15124217, 2022a.

365 Gao, W., Zhang, S., Li, X., and Liu, Z.: Investigation on the drag effect of a rolling element confined in the cavity of a cylindrical roller bearing, Proceedings of the Institution of Mechanical Engineers, Part J: Journal of Engineering Tribology, 236, 777–785, 2022b.

Gonda, A., Großberndt, D., Sauer, B., and Schwarze, H.: Experimental and numerical investigations of hydraulic losses in rolling bearings under practice-oriented conditions (Experimentelle und numerische untersuchungen der hydraulischen Verluste in Wälzlagern unter praxisrelevanten Bedingungen), Tribol. Schmier, 65, 7–13, 2018.

370 Gonda, A., Sauer, B., Großberndt, D., and Schwarze, H.: Experimental and numerical investigations of hydraulic losses in fully and partially flue , tapered roller bearings [experime tell und numerische untersuchungen der hydraulischen verluste in voll-und teilgefluteten kegelrollenlagern], VDI Berichte, 2348, 97–106, 2019.

Hoeprich, M. R.: Grease Performance in Tapered Roller Bearings, in: World Tribology Congress, vol. 42029, pp. 189–190, 2005.

Hong, S.-W. and Tong, V.-C.: Rolling-element bearing modeling: A review, International Journal of Precision Engineering and Manufactur-
375 ing, 17, 1729–1749, 2016.

Hu, J., Wu, W., Wu, M., and Yuan, S.: Numerical investigation of the air–oil two-phase flow inside an oil-jet lubricated ball bearing, International Journal of Heat and Mass Transfer, 68, 85–93, 2014.

Intergovernmental Panel on Climate Change: Climate Change 2022: Mitigation of Climate Change. Contribution of Working Group III to the Sixth Assessment Report of the Intergovernmental Panel on Climate Change, https://sdgs.un.org/sites/default/files/2023-01/IPCC_AR6_
380 WGIII_FullReport.pdf, accessed: 2025-04-28, 2022.

Ishaq Khan, M., Maccioni, L., and Concli, F.: Trends in Lubrication Research on Tapered Roller Bearings: A Review by Bearing Type and Size, Lubricant, and Study Approach, Lubricants, 13, https://www.mdpi.com/2075-4442/13/5/204, 2025.

Kaymaz, E., Duman, S., and Guvenc, U.: Optimal power flow solution with stochastic wind power using the Lévy coyote optimization algorithm, Neural Computing and Applications, 33, 6775–6804, 2021.

385 Khonsari, M. M. and Booser, E. R.: Applied Tribology: Bearing Design and Lubrication, John Wiley & Sons, Hoboken, NJ, 2017.

Li, M., Lu, F., Bai, X., Zhu, W., and Zhu, R.: Heat-flow coupling variation in double-row tapered-roller bearings during the loss of lubrication process, Proceedings of the Institution of Mechanical Engineers, Part C: Journal of Mechanical Engineering Science, 236, 7500–7510, 2022.

Liebrecht, J., Si, X., Sauer, B., and Schwarze, H.: Untersuchungen von hydraulischen Verlusten an Kegelrollenlagern, Tribologie und Schmierungstechnik, 62, 14–21, 2015.

Liebrecht, J., Si, X., Sauer, B., and Schwarze, H.: Berücksichtigung des Größeneinflusses bei der Berechnung der Plansch- und Schleppverluste an Wälzlagern, Tribologie und Schmierungstechnik, 64, 46–52, 2017.

Maccioni, L. and Concli, F.: Computational fluid dynamics applied to lubricated mechanical components: Review of the approaches to simulate gears, bearings, and pumps, Applied Sciences, 10, 8810, 2020.

Maccioni, L., Chernoray, V. G., Bohnert, C., and Concli, F.: Particle Image Velocimetry measurements inside a tapered roller bearing with an outer ring made of sapphire: Design and operation of an innovative test rig, Tribology International, 165, 107 313, 2022a.

Maccioni, L., Chernoray, V. G., Mastrone, M. N., Bohnert, C., and Concli, F.: Study of the impact of aeration on the lubricant behavior in a tapered roller bearing: Innovative numerical modelling and validation via particle image velocimetry, Tribology International, 165, 107 301, 2022b.

Maccioni, L., Chernoray, V. G., and Concli, F.: Fluxes in a full-flooded lubricated tapered roller bearing: particle image velocimetry measurements and computational fluid dynamics simulations, Tribology International, 188, 108 824, 2023a.

Maccioni, L., Rüth, L., Koch, O., and Concli, F.: Load-Independent Power Losses of Fully Flooded Lubricated Tapered Roller Bearings: Numerical and Experimental Investigation of the Effect of Operating Temperature and Housing Wall Distances, Tribology Transactions, 66, 1078–1094, 2023b.

Mang, T. and Dresel, W.: Lubricants and Lubrication, 2nd ed., Wiley-VCH, Weinheim, Germany, 2007.

Manjunath, M., Hausner, S., Heine, A., De Baets, P., and Fauconnier, D.: Electrical impedance spectroscopy for precise film thickness assessment in line contacts, Lubricants, 12, 51, 2024.

Marchesse, Y., Changenet, C., and Ville, F.: Drag power loss investigation in cylindrical roller bearings using CFD approach, Tribology Transactions, 62, 403–411, 2019.

Niemann, G. and Winter, H.: Getriebe Allgemein, Zahnradgetriebe—Grundlagen, Stirnradgetriebe, Maschinenelemente, Springer, Berlin/Heidelberg, Germany, 2002.

Raju, K., Veettil, M. P., Ray, S., and Shi, F.: Needle roller bearing lubricant flow CFD simulations, Tech. rep., SAE Technical Paper, 2013.

Ren, X., Xiao, Y., He, F., and Gozgor, G.: The contagion of extreme risks between fossil and green energy markets: evidence from China, Quantitative Finance, 24, 627–642, 2024.

Russell, T., Sadeghi, F., Peterson, W., Aamer, S., and Arya, U.: A novel test rig for the investigation of ball bearing cage friction, Tribology Transactions, 64, 943–955, 2021.

Santhosh, R., Hee, J. L., Simmons, K., Johnson, G., Hann, D., and Walsh, M.: Experimental investigation of oil shedding from an aero-engine ball bearing at moderate speeds, in: Turbo expo: power for land, sea, and air, vol. 50923, p. V07AT34A018, American Society of Mechanical Engineers, 2017.

Sun, Q. G., Wang, Y. F., Wang, Y., Niu, P., and Wang, X. S.: Numerical study on rolling bearing temperature field under the oil-air lubrication, Applied Mechanics and Materials, 487, 580–584, 2014.

Terwey, J. and Mendelin, J.: Design-to-cost for TRB-TRB wind turbine main bearing systems, Forschung im Ingenieurwesen, 89, 18, 2025.

Tong, V.-C. and Hong, S.-W.: Characteristics of tapered roller bearing subjected to combined radial and moment loads, International journal of precision engineering and manufacturing-green technology, 1, 323–328, 2014.

425 Versteeg, H. K.: An introduction to computational fluid dynamics the finite volume method, 2/E, Pearson Education India, 2007.

Wen, Y. and Oshima, S.: Oil flow simulation based on CFD for reducing agitation torque of ball bearings, SAE International Journal of Passenger Cars-Mechanical Systems, 7, 1385–1391, 2014.

Wu, W., Hu, C., Hu, J., and Yuan, S.: Jet cooling for rolling bearings: Flow visualization and temperature distribution, Applied Thermal Engineering, 105, 217–224, https://doi.org/https://doi.org/10.1016/j.applthermaleng.2016.05.147, 2016.

430 Zhang, S.-w.: Green tribology: Fundamentals and future development, Friction, 1, 186–194, 2013.

Zhu, W., Zhu, R., Tang, X., Lu, F., Bai, X., Wu, X., and Li, F.: CFD-based analysis of oil and gas two-phase flow characteristics in double-row tapered roller bearings with different rib structures, Applied Sciences, 12, 1156, 2022.